The Astrophysical Journal, 918:28 (11pp), 2021 September 1 https://doi.org/10.3847/1538-4357/ac0ae5

Eclipsing Binaries Found by the EREBOS Project: Gaia DR2 6097540197980557440—a Deeply Eclipsing sdB+dM System

Kyle A. Corcoran[1], Brad N. Barlow[2], Veronika Schaffenroth[3], Uli Heber[4], Stephen Walser[5], and Andreas Irgang[4]
[1] University of Virginia, Department of Astronomy, 530 McCormick Rd., Charlottesville, VA 22904, USA; kac8aj@virginia.edu
[2] High Point University, Department of Physics, One University Parkway, High Point, NC 27268, USA
[3] Universität Potsdam, Institut für Physik und Astronomie, Haus 28, Karl-Liebknecht-Str. 24/25, D-14476, Potsdam-Golm, Germany
[4] Dr. Karl Remeis-Observatory & ECAP, Astronomical Institute, Friedrich-Alexander University Erlangen-Nuremberg (FAU), Sternwartstr. 7, D-96049 Bamberg, Germany
[5] Virginia Tech, Department of Physics, 850 West Campus Drive, Blacksburg, VA 24061, USA
Received 2021 January 18; revised 2021 June 10; accepted 2021 June 11; published 2021 September 1

Abstract

We present time-series spectroscopy and photometry of Gaia DR2 6097540197980557440, a new deeply eclipsing hot subdwarf B (sdB) + M dwarf (dM) binary. We discovered this object during the course of the Eclipsing Reflection Effect Binaries from Optical Surveys (EREBOS) project, which aims to find new eclipsing sdB+dM binaries (HW Vir systems) and increase the small sample of studied systems. In addition to the primary eclipse, which is in excess of ∼5 mag in the optical, the light curve also shows features typical for other HW Vir binaries such as a secondary eclipse and strong reflection effect from the irradiated, cool companion. The orbital period is 0.127037 days (∼3 hr), falling right at the peak of the orbital period distribution of known HW Vir systems. Analysis of our time-series spectroscopy yields a radial velocity semiamplitude of $K_{\rm sdB} = 100.0 \pm 2.0\,{\rm km\,s^{-1}}$, which is among the fastest line-of-sight velocities found to date for an HW Vir binary. State-of-the-art atmospheric models that account for deviations from local thermodynamic equilibrium are used to determine the atmospheric parameters of the sdB. Although we cannot claim a unique light-curve modeling solution, the best-fitting model has an sdB mass of $M_{\rm sdB} = 0.47 \pm 0.03\,M_{\odot}$ and a companion mass of $M_{\rm dM} = 0.18 \pm 0.01\,M_{\odot}$. The radius of the companion appears to be inflated relative to theoretical mass–radius relationships, consistent with other known HW Vir binaries. Additionally, the M dwarf is one of the most massive found to date among this type of binary.

Unified Astronomy Thesaurus concepts: Eclipsing binary stars (444); Fundamental parameters of stars (555); B subdwarf stars (129)

1. Introduction

Most hot subdwarfs are core He-burning extreme horizontal branch stars that formed from red giant progenitors that experienced mass loss near the tip of the giant branch, due to binary interactions (see Heber 2016, for a detailed review). With temperatures from 20,000 to 45,000 K and spectra dominated by broad H Balmer lines, they are classified as either sdB stars or sdOB stars if they display the He II 4686 Å line. They show a tight mass distribution peaking near 0.47 $M_{\odot}$ (the "canonical" mass) and have radii around 0.2 $R_{\odot}$. Theoretical models such as those in Han et al. (2002, 2003) describe sdB formation scenarios that account for the mass loss in these systems, with three possible formation channels depending on the initial configuration and mass ratio of the binary. One formation channel produces an sdB via Roche lobe overflow to a main-sequence companion of K type and earlier. The binaries that form in this way are typically wide binaries ($P = 10$–1500 days). These systems are often called "composite" binaries, as both stars are seen in the spectrum and account for 30%–40% of all sdBs (for an overview see Vos et al. 2019). The rest of the sdBs do not show any signs of a companion in their spectra. Maxted et al. (2001) showed that a high fraction of those sdBs do exist in short-period binaries, leading to radial velocity (RV) variations. Those can be formed by common envelope (CE) evolution, which produces close binaries with periods as short as ∼1.5 hr with a hot subdwarf primary and a cool, low-mass companion. In this scenario, an evolving red giant and a companion object enter a CE, and the angular momentum resonant in the orbit of the binary is deposited into the envelope, ejecting it from the system. Typically, this companion is stellar in nature; however, Soker (1998) proposed that substellar and even planetary-mass companions could be sufficient to provide the orbital angular momentum necessary to eject the envelope (e.g., Schaffenroth et al. 2015). The remaining sdBs do not show any RV variations and hence appear single. Such single sdBs could be formed by the merger of two He white dwarfs (WDs). Another possibility is that a substellar companion was responsible for the mass loss, which was destroyed during the CE phase.

The main challenge in studying close sdB binaries and their properties comes from the single-lined nature of these systems, allowing only for mass limits inferred based on the proposed inclination; however, some systems benefit from the presence of an eclipse, which helps to constrain the inclination and allows for more precise mass measurements. These so-called HW Vir systems also show photometric variation due to the reflection effect and have orbital periods of $P < 1$ day, making them vital tools for sdB studies owing to the relative ease in identifying them. The prototypical HW Vir is an sdB and M dwarf (dM) binary. A few systems containing a brown dwarf (BD) have also been discovered (e.g., Schaffenroth et al. 2014a).

The Eclipsing Reflection Effect Binaries from Optical Surveys (EREBOS) project (Schaffenroth et al. 2019) is an effort to increase the sample of known HW Vir systems and to measure orbital, atmospheric, and fundamental parameters of those binaries. It is especially interested in finding the lower-mass limit of an object able to remove the envelope in a CE

phase and survive this phase in order to investigate the effect that substellar companions have on the late stages of stellar evolution. Moreover, this project aims at studying post-CE systems spanning the entire range of periods and companion masses for these systems. For a better understanding of the poorly understood CE phase, see Ivanova et al. (2013). Until recently, the number of HW Vir binaries with known fundamental parameters was relatively small at 18 total systems. The EREBOS project dramatically increased this number by inspecting light curves from the Optical Gravitational Lensing Experiment (OGLE; Pietrukowicz et al. 2013; Soszyński 2015) and Asteroid Terrestrial-impact Last Alert System (ATLAS; Tonry et al. 2018) surveys, finding over 150 new HW Vir candidates (Schaffenroth et al. 2019). With an extensive spectroscopic and photometric follow-up campaign we will dramatically increase the number of systems with robust solutions.

Despite this unprecedented increase, HW Vir systems still represent only a small fraction of the sdB population. Given the typical radii of both components, these systems have to be relatively edge-on to show any eclipse. For example, the smallest grazing eclipses occur in systems such ASAS 102322−3737 (Schaffenroth et al. 2013), an sdB+dM, at $i = 65.^{\circ}9$; however, inclinations do range up to perfectly edge-on systems such as AA Dor (Kilkenny et al. 1978), an sdOB+dM/BD. One HW Vir system, Konkoly J064029.1+385652.2 (Derekas et al. 2015), is an sdO+dM binary that even shows a total eclipse owing to a relatively small ($R = 0.096\,R_{\odot}$) sdO being in a nearly edge-on ($i = 87.11$) orbit with an inflated dM. Total eclipses are sometimes seen in WD+dM binaries such as NN Ser (Parsons et al. 2010), where a high inclination angle allows the dM to completely block the smaller WD along our line of sight. Due to the similarity in size between typical sdBs and dMs, even edge-on systems struggle to achieve geometries sufficient to produce a total eclipse.

Here we present system parameters for the first deeply eclipsing sdB+dM system Gaia DR2 6097540197980557440, which exhibits an eclipse in excess of ∼5 mag in the optical. We discovered Gaia DR2 6097540197980557440 in the course of the EREBOS project while obtaining follow-up observations of known HW Vir systems using the Goodman spectrograph (Clemens et al. 2004) on the 4.1 m Southern Astrophysical Research (SOAR). In Section 2 we describe the initial observations leading to its discovery. In Section 3 we present time-series spectroscopic observations, as well as the radial velocities and atmospheric parameters derived from them. In Section 4 we present multicolor, time-series photometric observations and the details of our light-curve modeling solution. Section 5 presents system parameters derived from the best-fitting light-curve modeling solution. In Section 6 we discuss how the system compares to the EREBOS sample, as well as potential follow-up studies. Finally, we summarize our work in Section 7.

2. Discovery Run

During a small amount of downtime between SOAR/Goodman observations of EREBOS targets on 2019 June 9, we discovered Gaia DR2 6097540197980557440 with approximately 45 minutes of time-series photometry using a Johnson V filter. We had previously identified Gaia DR2 6097540197980557440 as a strong candidate variable hot subdwarf from its anomalously high Gaia DR2 photometric uncertainty and its inclusion in the Geier et al. (2019) catalog of candidate hot subdwarf stars (for details see Barlow et al., in preparation; Guidry et al. 2021). We unwittingly began observing just before primary eclipse and, upon noticing the star disappear from the raw image frames[6] (shown in Figure 1), continued observing long enough to safely capture egress. Using the processes described in Section 4.1, we constructed a light curve and determined that the primary eclipse lasted approximately 25 minutes. The shape of the eclipse stuck out to us immediately as being different than in other HW Vir binaries. Whereas the ingress and egress segments of most primary eclipses have *positive* second time derivatives (i.e., concave up), Gaia DR2 6097540197980557440's second derivatives are *negative* during ingress and egress (i.e., concave down). This can only be explained by the geometry of a nearly perfectly edge-on eclipse, so we were eager to obtain photometry and spectroscopy over the full orbit to solve for all system parameters.

Unfortunately, we were unable to determine a precise orbital period for the system using our exploratory time-series photometry. However, Gaia DR2 6097540197980557440 was also observed by TESS in Sector 11 through full-frame image (FFI), 30-minute-cadence observations. The data[7] were downloaded from the Mikulski Archive for Space Telescopes (MAST) web portal, and the `lightkurve` (Lightkurve Collaboration et al. 2018) Python package was used to extract time-series photometry from the FFIs. A Lomb–Scargle periodogram (Scargle 1982) was computed and yielded an initial estimate of the system's orbital period of $P = 3.0614$ hr. This estimate helped guide subsequent observations.

3. Time-series Spectroscopy

3.1. Observations and Reductions

We obtained 53 spectra using SOAR/Goodman on 2019 July 25 and 46 spectra on 2020 February 17, both in an uninterrupted series of back-to-back exposures. Each of these data sets covered roughly 75% of the ∼3 hr orbital period. We used the $0.''8$-long slit, 2×2 binning, and the 930 mm^{-1} volume phase holographic grating (0.84 Å per binned pixel dispersion), giving us average spectral resolutions of 2.38 and 2.04 Å over the wavelength range 3600–5300 Å for the 2019 and 2020 data, respectively. We note that the spectral resolutions are different despite using the same instrumental configuration owing to the camera–collimator focus values not being set to their optimal values during the 2019 observations. On both observing nights, we aligned the slit axis to a position angle of $278.^{\circ}3$ E of N in order to place a bright star[8] $23.''5$ away on the slit and monitor any drifts in the wavelength solution due to instrumental flexure. Individual spectra in each series were integrated for 120 s, yielding an average signal-to-noise ratio (S/N) of ∼30 per resolution element. We also obtained spectra of FeAr lamps immediately following each series for wavelength calibration purposes.

Reduction of the frames was carried out using the `ccdproc` task in `IRAF` (Tody 1986, 1993). After bias-subtracting and flat-fielding all spectral images, we ran the `apall` task to extract a one-dimensional spectrum for each frame and remove a fit to the sky background. For the 2020 data, a wavelength solution was generated from the FeAr lamp spectra and applied to all individual spectra. We note that slow drifts in the

[6] At this moment, Stephen Walser, who was monitoring the frames as they came in, apologetically informed us he had "lost our star."
[7] Using the same data, Sahoo et al. (2020) concurrently found this object to be an eclipsing binary.
[8] Gaia DR2 6097528446950034944.

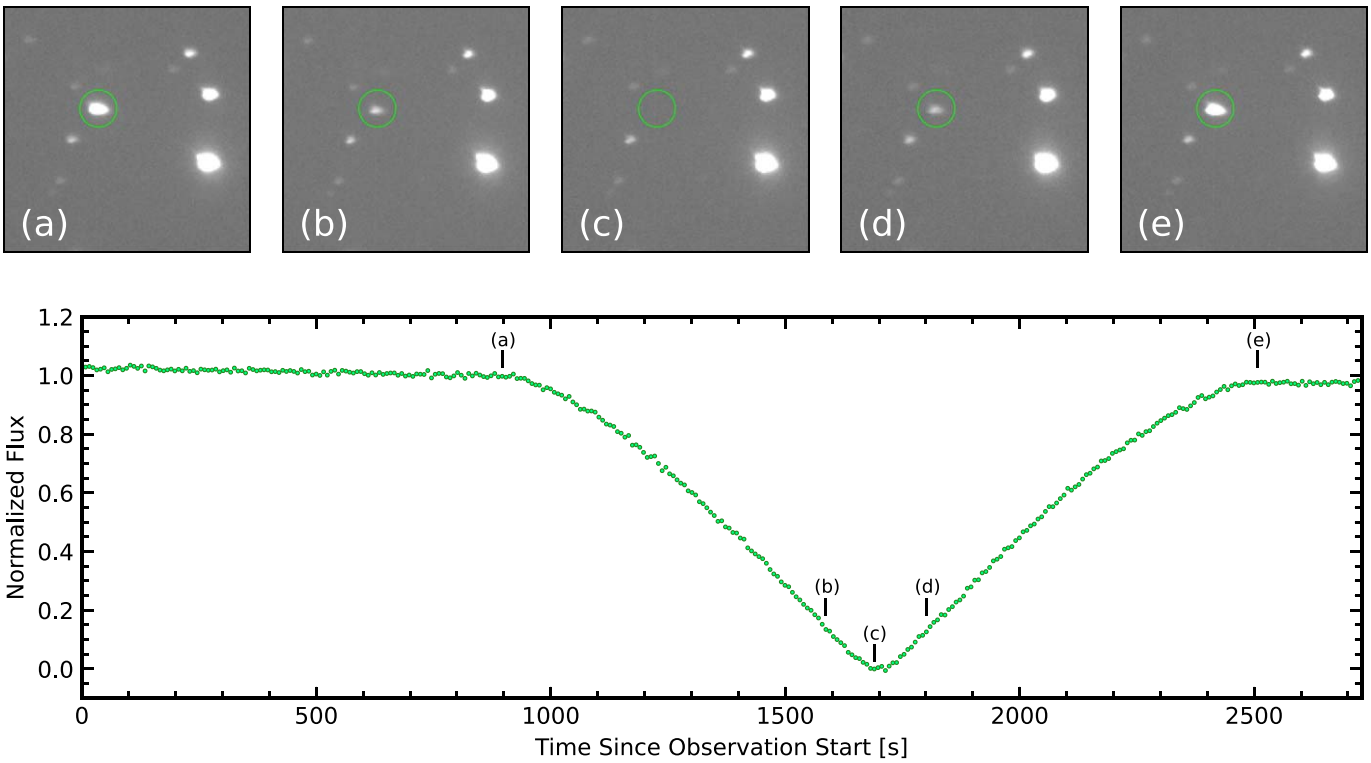

Figure 1. Discovery data for Gaia DR2 6097540197980557440 from SOAR/Goodman. Top: raw Johnson *V* filter frames from the discovery data set obtained on 2019 June 9. We highlight five select frames corresponding to the marked locations on the light curve in the bottom panel. These frames represent phases (a) just prior to ingress, (b) shortly before the systems drops below detection limits, (c) during primary eclipse totality, (d) shortly after the system returns above detection limits, and (e) just after egress. Bottom: the corresponding light curve of Gaia DR2 6097540197980557440 in the Johnson *V* filter.

wavelength solution over the course of the series are expected owing to instrumental flexure, and thus the FeAr wavelength solution does not provide an accurate zero-point—only an accurate dispersion solution. For the 2019 data, an intermittent issue with the FeAr lamp prevented us from obtaining an accurate dispersion solution with it. Instead, we created a self-template from the combined 2019 spectra and used the Balmer and He I lines to determine the wavelength solution. Once again, this only provides a dispersion solution and not an absolute RV zero-point. Consequently, we are unable to report on the binary's systemic velocity. The spectrum of Gaia DR2 6097540197980557440, shown in Figure 3, is dominated by strong H Balmer absorption features and weaker He I lines (4026, 4471, 4921, 5015 Å). The absence of the He II 4686 Å line rules out an sdOB classification.

3.2. Radial Velocity Curve

RV shifts were determined from nonlinear, least-squares fits of Gaussian profiles to the sdB H Balmer lines, which were carried out using the `curve_fit` function in the Python package `scipy` (Virtanen et al. 2020). The He I profiles were too noisy in individual spectra for this purpose. In order to correct for drifts in the wavelength solution (and thus drifts in the RVs) due to instrumental flexure during the observations, we also measured the relative velocity shifts of the absorption features of the second star on the slit. This object displayed spectral features consistent with a G/K-type star, and so we used the `crosscorrRV` function in the `PyAstronomy` library (Czesla et al. 2019) to measure velocity shifts via cross-correlation. The second star's RV curves revealed gradual, nearly linear shifts on the order of $\sim$75 km s^{-1} over $\sim$2 hr, in both the 2019 and 2020 data sets. The magnitude and pattern of these shifts—slightly different on the two nights—were consistent with expectations given the target's R.A., decl., average hour angle during each run, and associated Nasmyth cage rotations. We are confident that they are due to instrumental flexure and not intrinsic RV variations of the second star on the slit. To remove this flexure drift from the target RV curves, we fitted low-order polynomials to the comparison star's RV curves and subtracted this fit from the raw target star RV curves. The resulting RV curves are shown in Figure 2.

In order to determine the RV semiamplitude of the sdB ($K_{\rm sdB}$), we fitted sine waves to each of the data sets separately, with the orbital period and phase fixed to the values described in Section 4.2. From the 2019 July 25 data, we find $K_{\rm sdB} = 97.9 \pm 2.6$ km s^{-1}, and from the 2020 February 17 data, we derive $K_{\rm sdB} = 102.1 \pm 3.0$ km s^{-1}. These results agree within their 1σ uncertainties, and we adopt as our final RV semiamplitude their weighted average: $K_{\rm sdB} = 100.0 \pm 2.0$ km s^{-1}. The residuals in the bottom panels of Figure 2 are consistent with random noise and show that the data are consistent with a circular orbit, as expected for post-CE HW Vir binaries.

3.3. Atmospheric Parameters

For use in the spectroscopic analysis, model spectra are computed following the so-called hybrid approach (Przybilla et al. 2006a, 2006b; Nieva & Przybilla 2008). In this approach, deviations from local thermodynamic equilibrium (LTE) can be treated very efficiently using a combination of updated versions

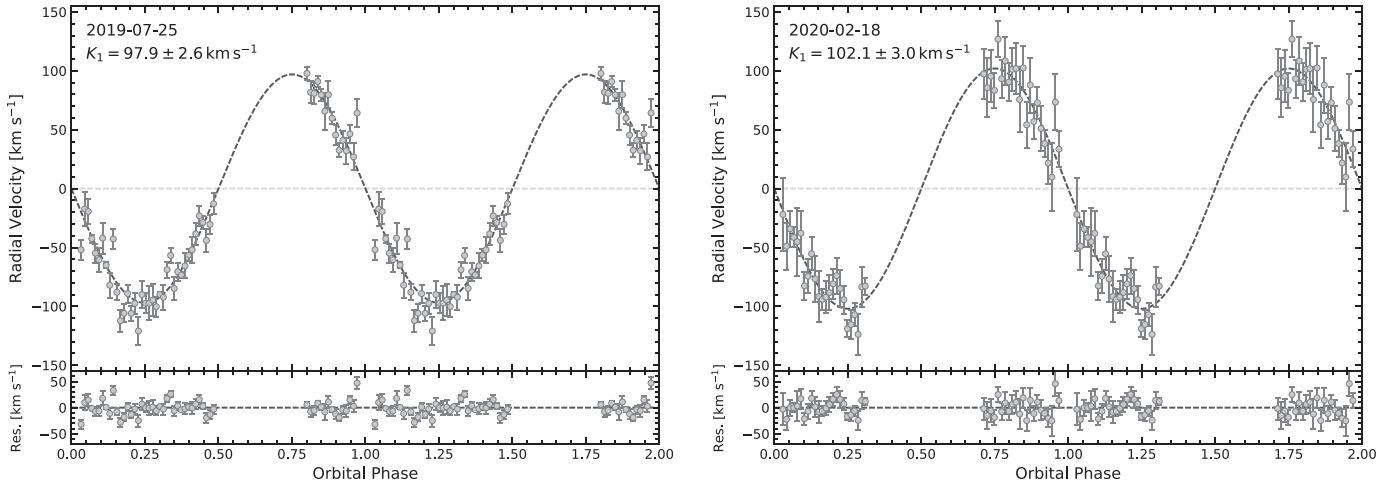

Figure 2. RV curves constructed from spectra obtained with SOAR/Goodman, plotted twice for better visualization. Left: best-fitting model for the data taken in 2019. Right: best-fitting model for the data taken in 2020. Both of these solutions agree within the error bars with the weighted average $K_{\mathrm{sdB}} = 100.0 \pm 2.0$ km s^{-1}.

of the ATLAS12 (Kurucz 1996), DETAIL (Giddings 1981; Butler & Giddings 1985), and SURFACE (Giddings 1981; Butler & Giddings 1985) codes. The ATLAS12 code, for which the mean metallicity for hot sdB according to Naslim et al. (2013) is used here, is initially used to compute the temperature/density structure of a line-blanketed, plane-parallel, and chemically homogeneous atmosphere in hydrostatic and radiative equilibrium. This LTE atmosphere is then used as input for the DETAIL code, which solves the coupled radiative transfer and statistical equilibrium equations to obtain occupation numbers in non-LTE (NLTE) for hydrogen and helium. Finally, the SURFACE code is used to compute the final synthetic spectrum using the atmosphere from ATLAS12 and the occupation numbers from DETAIL, as well as more sophisticated line-broadening data. Also taken into consideration are the recent improvements to all three codes (Irrgang et al. 2018) concerning NLTE effects on the atmospheric structure, the implementation of the occupation probability formalism (Hubeny et al. 1994) for hydrogen and neutral helium, and new Stark broadening tables for hydrogen (Tremblay & Bergeron 2009) and neutral helium (Beauchamp et al. 1997). The application of these models to sdBs is also shown in Schaffenroth et al. (2021).

The observed spectra are matched to the model grid by χ^2 minimization as described by Saffer et al. (1994) as implemented by Napiwotzki et al. (1999). We use six H Balmer lines and four He I lines. H ϵ is excluded because of contamination by interstellar Ca II. Since the binary orbit is so tight, tidal forces probably have spun up the sdB star, which causes extra line broadening. However, the resolution of the spectra is insufficient to measure the projected rotational velocity $v \sin i$. We assume that the rotation of the sdB is tidally locked to the binary orbit and convolve the model spectrum with a rotational broadening profile with a corresponding $v \sin i = 87$ km s^{-1} in the fitting procedure.

Previous studies have shown that some sdBs with reflection effects have atmospheric parameters that can vary with phase when analyzing spectra of sufficiently high S/N taken at different phases of the orbit (e.g., Schaffenroth et al. 2013, 2014b). These variations can be explained by the companion's phase-variable contributions to the spectrum from only the reflection effect, causing apparent variations of order 1000–1500 K and 0.1 dex in the sdB temperature and surface gravity, respectively.

To account for any of these variations, we derived the atmospheric parameters from the single-RV-corrected spectra. Exemplary fits are shown for individual spectra from the 2019 and 2020 observing runs for similar orbital phases in Figure 3. Results from both observing runs are consistent. The variations of the atmospheric parameters, which are consistent with previous determinations, can be seen in Figure 4. The effective temperature appears to increase slightly near the secondary eclipse. Any variations in the surface gravity or helium abundance remain below detection limits. In order to determine the atmospheric parameters of the sdB, we averaged the parameters near the primary eclipse, where only the dark side of the companion is visible: $T_{\mathrm{eff}} = 26100 \pm 400$ K, $\log(g) = 5.50 \pm 0.07$, and $\log(y) = -2.32 \pm 0.10$.

4. Time-series Photometry

4.1. Observations and Reductions

Follow-up time-series photometry was obtained on 2020 February 18 using SOAR/Goodman in imaging mode. In an effort to obtain multicolor photometry for more precise modeling, the filter wheel was manually switched between the Johnson B and R filters every few minutes when not in primary or secondary eclipse, and every 30 s during eclipses. The integration time was fixed to 5 s for both filters in order to minimize dead time and errors associated with changing this value back and forth every few minutes. We used 2×2 binning and read out only a 350×175 binned pixel subset of the image to minimize the readout time between exposures. This relatively small field still provided several nearby comparison stars through which to track sky transparency variations. We achieved a duty cycle of roughly 54% over the course of our observations, which covered a little more than one full orbital period. A more efficient duty cycle would have required either decreasing the subframe region further and sacrificing comparison stars or increasing the exposure time and risk saturating the target and comparison stars.

Reduction of the SOAR frames was once again carried out using the `ccdproc` procedure in `IRAF`. Each raw image frame was first bias-subtracted and flat-fielded. We then extracted aperture photometry using a range of aperture sizes with a

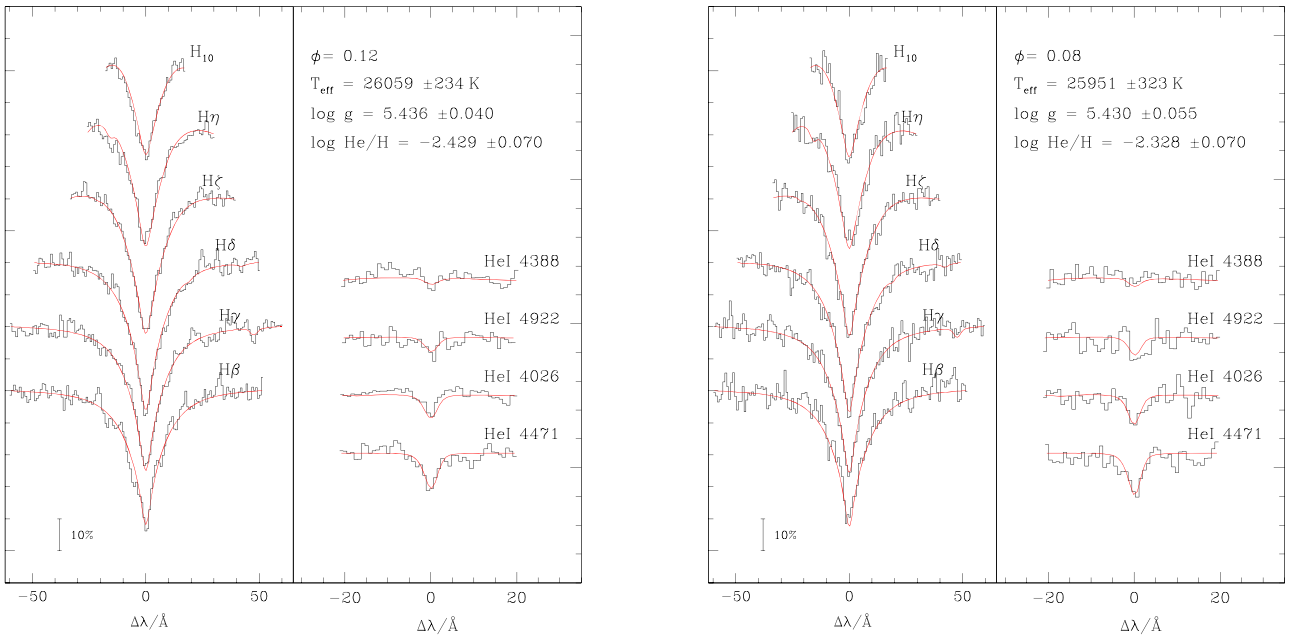

Figure 3. Line fits to the hydrogen Balmer and neutral helium lines in individual SOAR/Goodman spectra from 2019 (left panel) and 2020 (right panel). Listed in the upper right corner of each panel is the orbital phase and the resulting set of best-fitting atmospheric parameters.

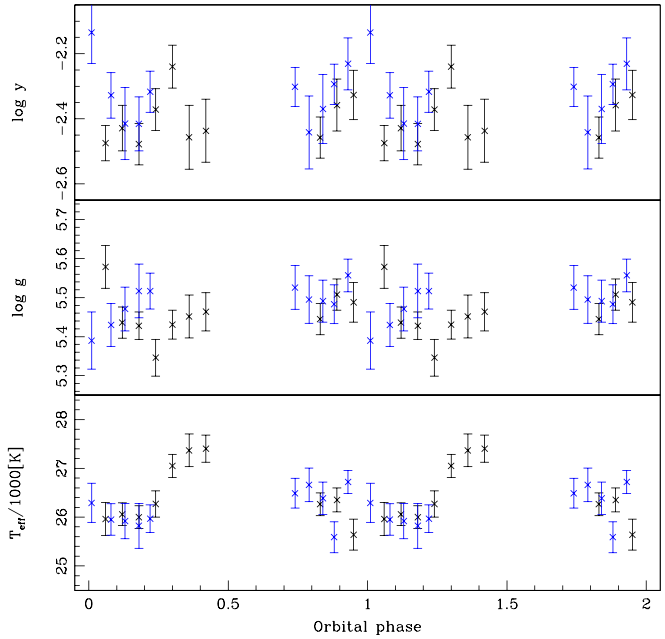

Figure 4. Apparent $T_{\rm eff}$ (bottom), $\log g$ (middle), and $\log y$ (top) variations with 1σ error bars as a function of the orbital phase. Results from spectra taken in 2019 are shown in black, while those from 2020 are shown in blue.

custom code utilizing the `photutils` (Bradley et al. 2019) Python package. Sky counts were removed using sky annuli drawn around the apertures. Apertures were chosen to maximize the S/N in each light curve. This process was repeated on multiple nearby, bright comparison stars to remove sky transparency variations and flux-normalize the light curves. Multiple cycles of observing are typically needed to remove air-mass-related changes in the flux; therefore, any of these slight flux variations were not removed during the reduction process. The resulting differential light curves are shown in Figure 5 and used for modeling the binary.

4.2. Binary Light-curve Modeling

The Gaia DR2 6097540197980557440 light curve exhibits all the typical HW Vir features. The amplitude of the reflection effect is noticeably stronger in the *R* filter (∼30%) than in the *B* filter (∼20%), and it is quite strong in general compared to other reflection effect systems. Initially, this led us to believe that either the sdB was slightly hotter than in typical HW Vir systems or the companion was slightly larger than usual. The deep primary eclipse, implying a nearly edge-on inclination, lent credence to the latter explanation. The shape of the eclipse itself sticks out among other HW Vir binaries. As mentioned in Section 2, the ingress and egress segments of the primary eclipse have negative second derivatives (more V shaped) instead of the more frequently observed positive second derivatives (more U shaped). This implies that the eclipse geometry is nearly perfectly edge-on and that the companion might be slightly larger than the primary. Secondary eclipses are also present in the light curve, during which the sdB is blocking irradiated light from the cool companion. Notably, the flux at the center of the secondary eclipse returns to its exact value immediately preceding and following ingress and egress, respectively, further implying that the inclination must be nearly edge-on.

To model the light curves, we use the code `LCURVE` (for details, see Appendix A in Copperwheat et al. 2010). In addition to recreating deep eclipses, `LCURVE` was designed for binaries with WDs and has been used to fit WD+dM systems exhibiting the reflection effect (e.g., Parsons et al. 2010); therefore, HW Vir binaries are naturally suited to be modeled in a similar fashion (see Schaffenroth et al. 2021, for an example and further details). To form full solutions for these systems, there are many parameters that are not all independent, so we can greatly improve our ability to constrain each solution by fixing as many parameters as possible. We fixed the sdB temperature to the value determined in our spectroscopic fit (described in Section 3.3). We also fix the gravitational limb-darkening coefficients to values expected of a primary with a

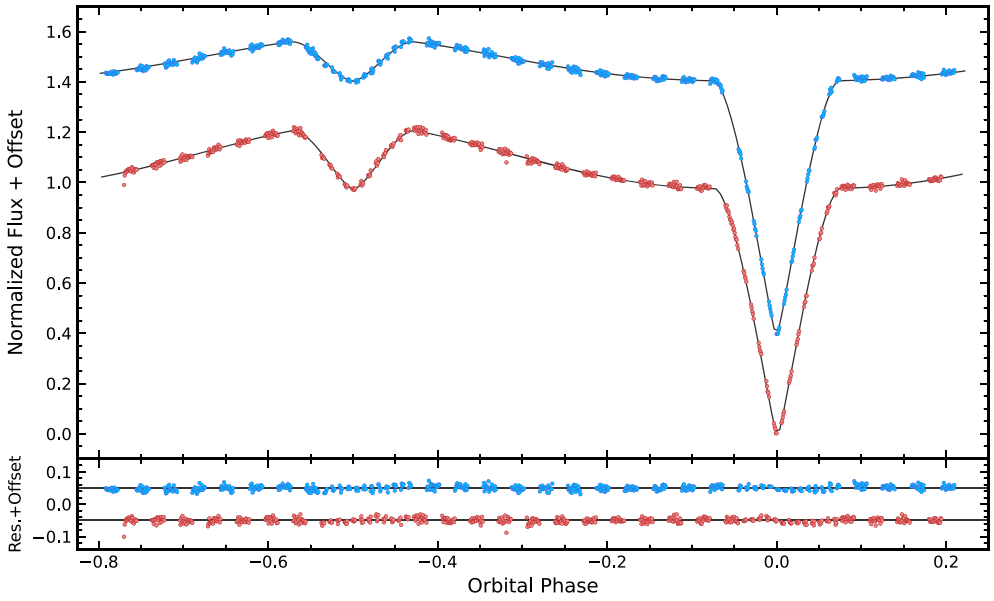

Figure 5. SOAR/Goodman light curves of Gaia DR2 6097540197980557440 in both the Johnson *B* (blue points) and *R* (red points) filters, along with their respective best-fitting models from Section 4.2. The *B*-filter light curve is offset by 0.4 for better visualization. Residuals are shown in the bottom panel with offsets of 0.05 and −0.05 for the *B* and *R* curves, respectively.

radiative atmosphere (von Zeipel 1924) and a companion with a convective atmosphere (Lucy 1967) by calculating the resulting intensities using a blackbody approximation. Then, we adopted a quadratic limb-darkening law for the primary using the values in Claret & Bloemen (2011) closest to the parameters derived in our spectroscopic fits.

It is important to note that there is a large degeneracy in the light-curve solutions of HW Vir binaries, even when fixing all of the above parameters. The orbit is certainly almost circular, so each model is not sensitive to the mass ratio (q) of the system. For this reason we calculated different solutions over a range of various, fixed mass ratios. We then use a SIMPLEX algorithm (Press et al. 1992) to vary parameters such as the inclination, both radii, the companion's temperature, albedo, and limb darkening, and even the period and primary eclipse time to help localize the solutions. Additionally, we allow for linear trends due to air-mass-related changes in flux over the course of the observations.

Next, we tested the degeneracy of each light-curve solution and determined the parameter errors by performing Markov Chain Monte Carlo computations using `emcee` (Foreman-Mackey et al. 2013). We used the best-fit solution from our SIMPLEX algorithm for initial values, and then we again varied the inclination angle, both radii, the limb-darkening coefficient assuming a linear limb-darkening law for the companion, and the companion's temperature and albedo for the mass ratio of our most probable solution (see Section 5). In all cases, the temperature of the companion is not well constrained, as its fractional luminosity contribution to the system—outside of the reflection effect—is negligible. We therefore constrained the companion's temperature to the range 2500–3500 K (the expected range for the low-mass companion). The results and errors from our `emcee` run (shown in Table 1) then form the basis for our most probable solution.

4.3. Orbital Ephemeris

To aid in future observations of Gaia DR2 6097540197980557440, we have listed its orbital ephemeris (T_0, P) in Table 2. We adopt the orbital period from our best-fit `emcee` solution in Section 4.2. To construct an initial eclipse time (T_0), we fit inverted Gaussian profiles to both the *B* and *R* time-series data using `curve_fit`. We then adopt the weighted average of the central times from both filter series as our T_0 value.

5. System Parameters

In Figure 6, we plot the surface gravity and sdB mass for each of the potential solutions, and we compare the photometric surface gravities to our spectroscopically derived surface gravity.

Based on the spectroscopic surface gravity, we get a consistent solution for an sdB mass of 0.3–0.64 $M_\odot$. All possible solutions fit the light-curve data nearly equally well; thus, we cannot claim a unique solution without additional data (e.g., velocity measurements from the dM). The most probable solution is the one with an sdB mass consistent with the canonical mass of 0.47 $M_\odot$. The adopted best-fitting light-curve solution and all relevant parameters are given in Table 1, and both of these best-fit models are shown together with their respective observations and residuals in Figure 5. All possible solutions are given in Table 3 of the Appendix.

We compute the binary mass function for Gaia DR2 6097540197980557440 using the expression

$$f = \frac{K_{\rm sdB}^3 P}{2\pi G} = \frac{M_{\rm sdB} q^3 \sin^3 i}{(1+q)^2}, \quad (1)$$

finding $f = 0.0132 \pm 0.0008$ $M_\odot$ using the period and sdB velocity semiamplitude. Combining this with the adopted mass ratio derived before, we find the sdB and dM masses to be $M_{\rm sdB} = 0.47 \pm 0.03\,M_\odot$ and $M_{\rm dM} = 0.18 \pm 0.01\,M_\odot$, respectively.

Table 1
Parameters Used to Model the Light Curve for Both the SOAR/Goodman *B* and *R* Data

Parameter	SOAR/Goodman—*B*	SOAR/Goodman—*R*	Unit	Description
		Fixed Parameters		
q ($M_{\rm dM}/M_{\rm sdB}$)	0.375	0.375		Mass ratio
P	0.127037	0.127037	days	Orbital period
$T_{\rm sdB}$	26100	26100	K	Primary temperature from spectroscopy
g_1	0.25	0.25		Gravitational darkening exponent
g_2	0.08	0.08		Gravitational darkening exponent
$x_{1,a}$	0.097	0.070		Primary linear limb-darkening coefficient
$x_{1,b}$	0.285	0.222		Primary quadratic limb-darkening coefficient
		Adjusted Parameters		
i	$90^{+0.0}_{-0.3}$	$90^{+0.0}_{-0.4}$	deg	Inclination angle
$x_{2,a}$	0.2992	0.2734		Companion linear limb-darkening coefficient
$R_{\rm sdB}/a$	0.2180 ± 0.0007	0.2174 ± 0.0007		Primary radius
$R_{\rm dM}/a$	0.2402 ± 0.0006	0.2407 ± 0.0006		Companion radius
$T_{\rm dM}$	2800 ± 500	3100 ± 500	K	Companion temperature
A_2	1.14 ± 0.01	1.4 ± 0.01		Companion albedo (absorb)
m	0.00026 ± 0.00001	0.00026 ± 0.00001		Slope

Table 2
Overview of Derived Parameters for Gaia DR2 6097540197980557440 That Represent the Most Probable Solution from the Set of Potential Solutions

Parameter	Value	Unit
	Basic Information	
α[a,b]	213.577775581303	deg
δ[a,b]	−43.552249057309	deg
G[a]	16.358994	mag
$G_{\rm bp} - G_{\rm rp}$[a]	−0.27529526	mag
	System Properties	
T_0	$2{,}458{,}898.85724 \pm 0.00003$	BJD
P	0.127037 ± 0.000001	days
i	$90^{+0.0}_{-0.3}$	deg
q	0.375 ± 0.003	
a	0.921 ± 0.018	$R_\odot$
	sdB Properties	
$M_{\rm sdB}$	0.47 ± 0.03	$M_\odot$
$R_{\rm sdB}$	0.199 ± 0.004	$R_\odot$
$T_{\rm eff}$	$26{,}100 \pm 400$	K
$\log(g)$	5.50 ± 0.07	
$\log(y)$	-2.32 ± 0.10	
$K_{\rm sdB}$	100.0 ± 2.0	km s^{-1}
	dM Properties	
$M_{\rm dM}$	0.177 ± 0.010	$M_\odot$
$R_{\rm dM}$	0.222 ± 0.004	$R_\odot$
$T_{\rm eff}$	3000 ± 500	K

Notes.
[a] From Gaia DR2 (Gaia Collaboration et al. 2018).
[b] Epoch J2015.5.

Using Kepler's third law, we then find the orbital separation to be $a = 0.921 \pm 0.018\,R_\odot$. We also find $R_{\rm sdB} = 0.199 \pm 0.004\,R_\odot$ and $R_{\rm dM} = 0.222 \pm 0.004\,R_\odot$. Table 2 gives an overview of the adopted parameters for Gaia DR2 6097540197980557440.

In Figure 7, we show each set of parameters for the companion and the theoretical mass–radius relations for low-mass main-sequence stars from Baraffe et al. (2015) as an additional check. It is clear that each solution yields a companion radius that is inflated relative to what is predicted by theory, which is a trend commonly seen in close binaries with M dwarf components (Parsons et al. 2018). For our most probable solution we get a companion inflation of about ∼13%.

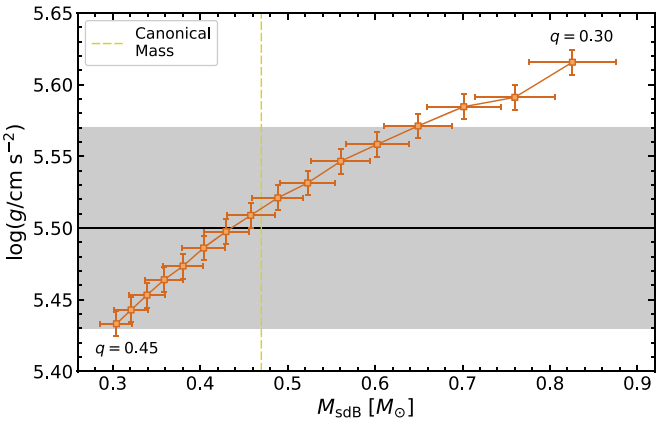

Figure 6. Photometric surface gravities plotted against their respective sdB masses for different mass ratio solutions ranging from $q = 0.3$ to 0.45, in 0.01 increments. The solid horizontal line (black) and shaded area represent the spectroscopically derived $\log(g)$ and associated 1σ error, respectively. The vertical dashed line (yellow) represents the canonical sdB mass of 0.47 $M_\odot$. The intersection of these two lines shows that our most probable solution is the one with an sdB mass just below the canonical mass.

6. Discussion

Our analysis of Gaia DR2 6097540197980557440 represents the first EREBOS case study following the Schaffenroth et al. (2019) report of newly discovered sdB+dM systems. With each additional system that is solved, EREBOS comes one step closer to achieving one of its goals to make statistical statements about a homogeneously selected population of close sdB systems. While one new system by itself might not push the boundaries of key parameters in these studies, each system provides self-consistent feedback about the methodology used

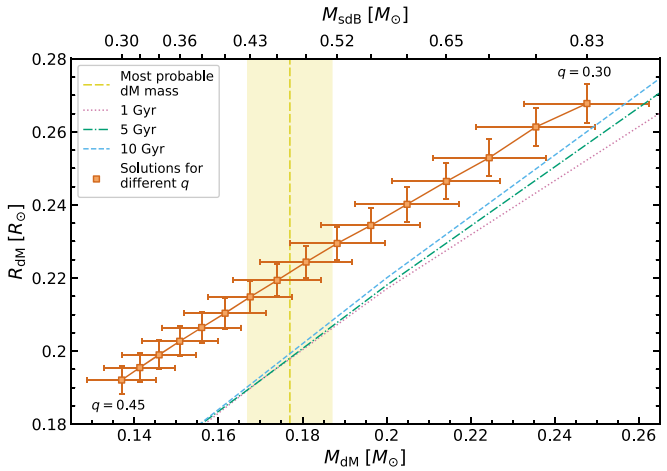

Figure 7. Mass–radius diagram for the dM companion illustrating the degeneracy in model solutions (orange squares). Theoretical mass–radius relations of low-mass stars (Baraffe et al. 2015) for 1 Gyr (dashed blue line), 5 Gyr (dashed–dotted green line), and 10 Gyr (dotted pink line) are also included. The vertical yellow line and shaded region represent the most probable dM mass and 1σ error, respectively, associated with the adopted 0.47 $M_\odot$ sdB solution.

to study the overall population. It is only through these self-consistent measures that EREBOS can eventually make statements regarding the effects stellar and substellar companions have on the late stages of stellar evolution.

Our light-curve and atmospheric modeling solutions imply that Gaia DR2 6097540197980557440 is a fairly typical sdB+dM system, aside from the chance alignment of its orbital plane nearly perfectly along our line of sight. The peak of the EREBOS orbital period distribution for both new and previously published systems from Schaffenroth et al. (2019) is at $P = 0.1$ days, meaning that Gaia DR2 6097540197980557440 falls at the typical period for HW Vir systems. The most probable solution is an sdB with a mass of the canonical mass $M_{sdB} = 0.47 \pm 0.03\,M_\odot$. Additionally, our derived $\log(g)$ and $\log(y)$ values are also fairly typical of sdBs in HW Vir systems, but it is worth noting that our T_{eff} value is slightly lower than is typically found (for comparison, see Figure 6 in Schaffenroth et al. 2019).

There are also noteworthy aspects of the system that are somewhat atypical among HW Vir systems, namely, the derived companion mass and sdB velocity semiamplitude. The companion mass is tied for the most massive in an HW Vir binary, along with that of Konkoly J064029.1+385652.2—also a deeply eclipsing HW Vir–type (sdO+dM) binary. Gaia DR2 6097540197980557440 has an orbital period that is ~1.5 hr shorter than Konkoly J064029.1+385652.2 and will one day evolve into a more rapid analog of Konkoly J064029.1 +385652.2 when the sdB evolves into an sdO after the He in the core is exhausted and then, inevitably, into a WD. The sdB semiamplitude we derive from the two sets of RV data makes Gaia DR2 6097540197980557440 the fastest line-of-sight sdB velocity semiamplitude reported to date for an HW Vir binary.

The most striking aspect of Gaia DR2 6097540197980557440 is the total eclipse of the sdB by its companion. Due to this system being relatively bright ($G \sim 16.4$ mag), a large eclipse depth means future eclipse timing ($O - C$) analyses to search for changes in the orbital period ($\dot{P}$), and even Rømer delay studies should be possible using telescopes with a variety of aperture sizes (e.g., Barlow et al. 2012). Additionally, Gaia DR2 6097540197980557440 will be observed at 2-minute cadence in Sector 38 of TESS Cycle 3 through the Guest Investigator program (proposal #G03221), providing space-quality data spanning 27 days of observations. This is a unique opportunity to explore a relatively novel parameter space with one of the most accurate astrophysical clocks known (e.g., Kilkenny 2014).

7. Summary

We have presented photometric and spectroscopic observations of Gaia DR2 6097540197980557440, the first deeply eclipsing sdB+dM binary. Other than the remarkably striking nature of the eclipse, the system is a rather typical sdB+dM system. We find an orbital period of $P = 0.127037$ days and an sdB velocity semiamplitude of $K_{sdB} = 100.0\,\mathrm{km\,s^{-1}}$, which, combined with the most probable light-curve solution, yields masses of $M_{sdB} = 0.47\,M_\odot$ and $M_{dM} = 0.18\,M_\odot$, respectively. This gives a radius of $R_{dM} = 0.222\,R_\odot$ for the companion, which is slightly inflated relative to theoretical mass–radius relationships of low-mass main-sequence stars. Gaia DR2 6097540197980557440 represents the first HW Vir solved as part of the EREBOS project. Eventual solutions for the more than 100 new HW Vir binaries uncovered by EREBOS will help improve our understanding of the CE channel leading to sdBs and help determine the effects nearby low-mass stellar and substellar objects can have on stars climbing the giant branch.

K.A.C., B.N.B., and S.W. acknowledge the support of the National Science Foundation under grant AST-1812874. B.B. also acknowledges partial support of this work by NASA through the TESS Guest Investigator program, under grant 80NSSC19K1720. V.S. is supported by the Deutsche Forschungsgemeinschaft (DFG) through grant GE 2506/9-1. A.I. acknowledges funding by the DFG through grant HE1356/70-1.

This research draws on data provided by NOIRLab 2019A-0255 and 2020A-0268; PI B. Barlow as distributed by the NOIRLab Astro Data Archive. NOIRLab is managed by the Association of Universities for Research in Astronomy (AURA) under a cooperative agreement with the National Science Foundation.

Based on observations obtained at the Southern Astrophysical Research (SOAR) telescope, which is a joint project of the Ministério da Ciência, Tecnologia, Inovações e Comunicações (MCTIC) do Brasil, the U.S. National Optical Astronomy Observatory (NOAO), the University of North Carolina at Chapel Hill (UNC), and Michigan State University (MSU).

This paper includes data collected with the TESS mission, obtained from the MAST data archive at the Space Telescope Science Institute (STScI). Funding for the TESS mission is provided by the NASA Explorer Program. STScI is operated by the Association of Universities for Research in Astronomy, Inc., under NASA contract NAS 5-26555.

This research made use of Lightkurve, a Python package for Kepler and TESS data analysis (Lightkurve Collaboration et al. 2018). This research made use of Photutils, an Astropy package for detection and photometry of astronomical sources (Bradley et al. 2019).

Appendix

Shown in Figures 8 and 9 are the corner plots for the SOAR/Goodman *B* and *R* light-curve solutions, respectively, using the Python package `corner` (Foreman-Mackey 2016) for visualization. Also, we give the full set of possible solutions from the light-curve modeling in Table 3.

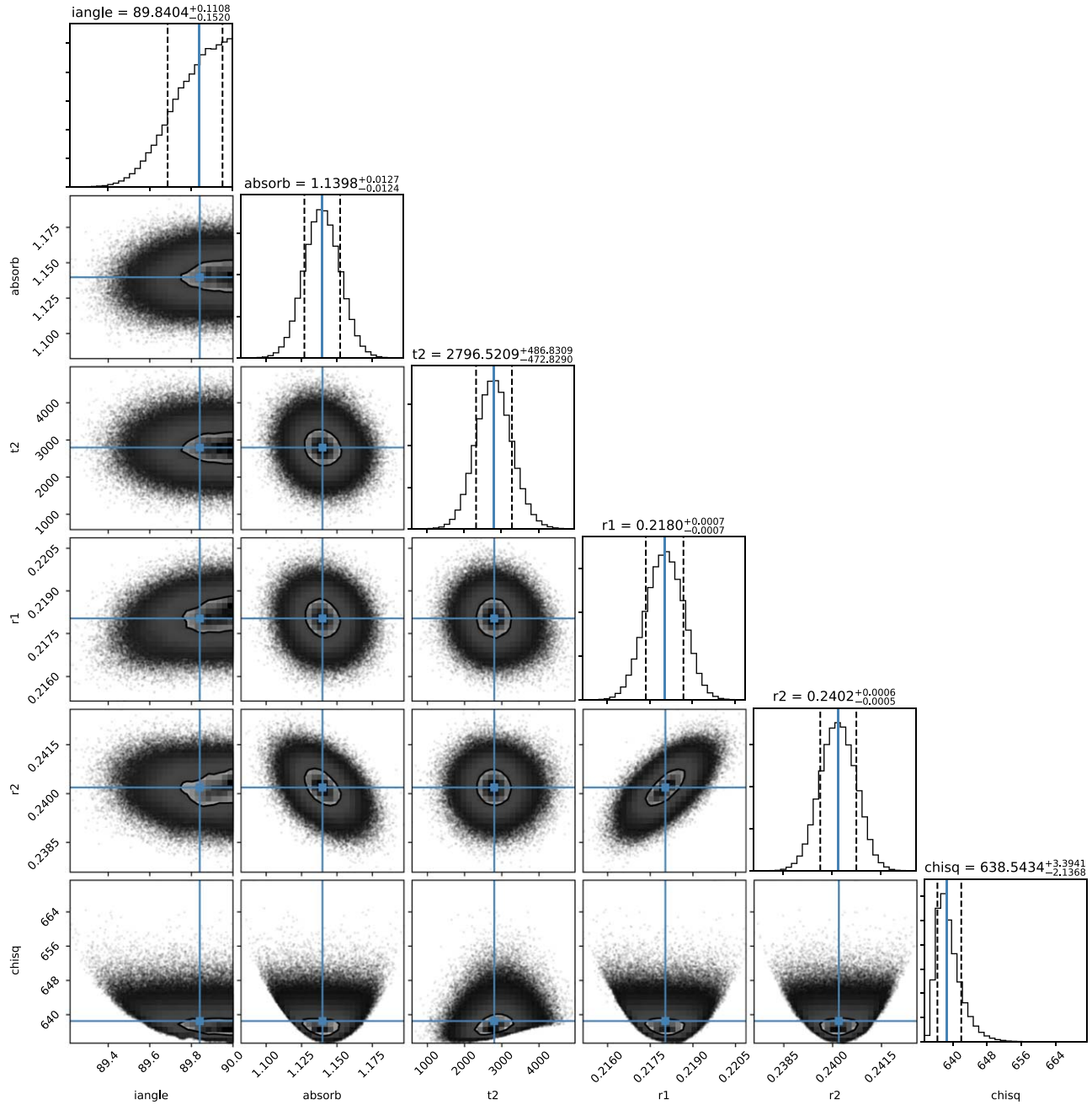

Figure 8. Corner plot of the most probable light-curve solution for the SOAR/Goodman—*B* data.

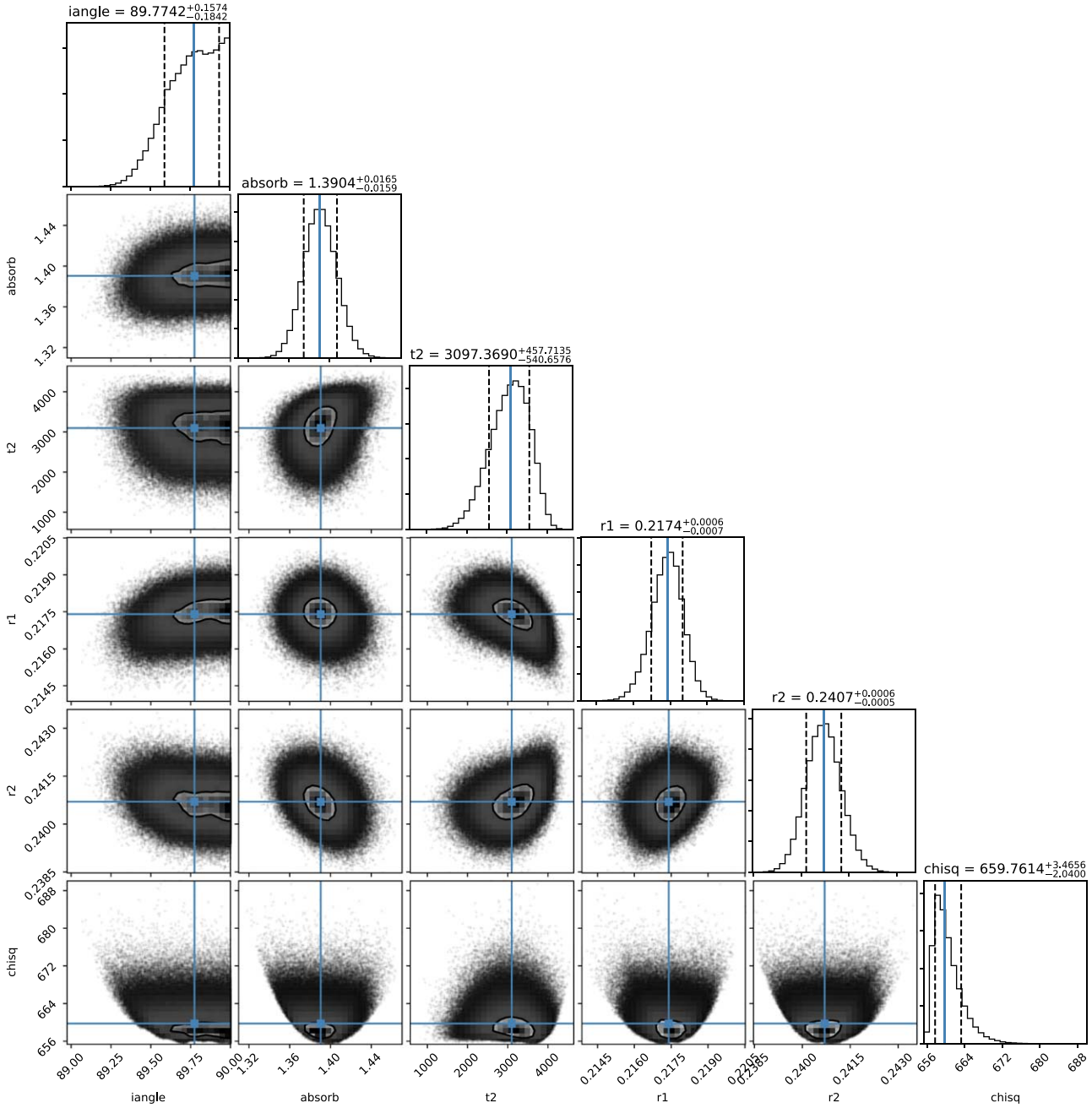

Figure 9. Corner plot of the most probable light-curve solution for the SOAR/Goodman—*R* data.

Table 3
All of the Possible Light-curve Solutions Output by LCURVE

q	a ($R_\odot$)	$M_{\rm sdB}$ ($M_\odot$)	$M_{\rm dM}$ ($M_\odot$)	$R_{\rm sdB}$ ($R_\odot$)	$R_{\rm dM}$ ($R_\odot$)	$\log(g)$
0.30	1.090 ± 0.022	0.826 ± 0.050	0.248 ± 0.015	0.234 ± 0.005	0.268 ± 0.005	5.616 ± 0.009
0.31	1.063 ± 0.021	0.760 ± 0.046	0.236 ± 0.014	0.231 ± 0.005	0.261 ± 0.005	5.591 ± 0.009
0.32	1.038 ± 0.021	0.701 ± 0.042	0.224 ± 0.013	0.224 ± 0.004	0.253 ± 0.005	5.585 ± 0.009
0.33	1.014 ± 0.020	0.649 ± 0.039	0.214 ± 0.013	0.219 ± 0.004	0.246 ± 0.005	5.571 ± 0.009
0.34	0.992 ± 0.020	0.603 ± 0.036	0.205 ± 0.012	0.214 ± 0.004	0.240 ± 0.005	5.558 ± 0.009
0.35	0.971 ± 0.019	0.561 ± 0.034	0.196 ± 0.012	0.209 ± 0.004	0.234 ± 0.005	5.547 ± 0.009
0.36	0.951 ± 0.019	0.523 ± 0.031	0.188 ± 0.011	0.205 ± 0.004	0.229 ± 0.005	5.531 ± 0.009
0.37	0.932 ± 0.019	0.489 ± 0.029	0.181 ± 0.011	0.201 ± 0.004	0.224 ± 0.004	5.521 ± 0.009
0.38[a]	0.914 ± 0.018	0.458 ± 0.027	0.174 ± 0.010	0.197 ± 0.004	0.219 ± 0.004	5.509 ± 0.009
0.39	0.897 ± 0.018	0.430 ± 0.026	0.168 ± 0.010	0.194 ± 0.004	0.215 ± 0.004	5.497 ± 0.009
0.40	0.881 ± 0.018	0.404 ± 0.024	0.162 ± 0.010	0.190 ± 0.004	0.210 ± 0.004	5.486 ± 0.009
0.41	0.865 ± 0.017	0.380 ± 0.023	0.156 ± 0.009	0.187 ± 0.004	0.206 ± 0.004	5.473 ± 0.009
0.42	0.851 ± 0.017	0.359 ± 0.022	0.151 ± 0.009	0.184 ± 0.004	0.203 ± 0.004	5.464 ± 0.009
0.43	0.837 ± 0.017	0.339 ± 0.020	0.146 ± 0.009	0.181 ± 0.004	0.199 ± 0.004	5.453 ± 0.009
0.44	0.824 ± 0.016	0.321 ± 0.019	0.141 ± 0.008	0.178 ± 0.004	0.195 ± 0.004	5.443 ± 0.009
0.45	0.811 ± 0.016	0.304 ± 0.018	0.137 ± 0.008	0.175 ± 0.004	0.192 ± 0.004	5.433 ± 0.009

Note.
[a] Most probable solution as outlined in the text.

ORCID iDs

Kyle A. Corcoran https://orcid.org/0000-0002-2764-7248
Brad N. Barlow https://orcid.org/0000-0002-8558-4353
Veronika Schaffenroth https://orcid.org/0000-0001-6339-6768
Uli Heber https://orcid.org/0000-0001-7798-6769
Stephen Walser https://orcid.org/0000-0001-8444-2305
Andreas Irgang https://orcid.org/0000-0002-0465-3725

References

Baraffe, I., Homeier, D., Allard, F., & Chabrier, G. 2015, A&A, 577, A42
Barlow, B. N., Wade, R. A., & Liss, S. E. 2012, ApJ, 753, 101
Beauchamp, A., Wesemael, F., & Bergeron, P. 1997, ApJS, 108, 559
Bradley, L., Sipőcz, B., Robitaille, T., et al. 2019, astropy/photutils: v0.6, Zenodo, doi:10.5281/zenodo.2533376
Butler, K., & Giddings, J. R. 1985, Newsletter of Analysis of Astronomical Spectra, No. 9 (London: Univ. College London)
Claret, A., & Bloemen, S. 2011, A&A, 529, A75
Clemens, J. C., Crain, J. A., & Anderson, R. 2004, Proc. SPIE, 5492, 331
Copperwheat, C. M., Marsh, T. R., Dhillon, V. S., et al. 2010, MNRAS, 402, 1824
Czesla, S., Schröter, S., Schneider, C. P., et al. 2019, PyA: Python astronomy-related packages,Astrophysics Source Code Library, ascl:1906.010
Derekas, A., Németh, P., Southworth, J., et al. 2015, ApJ, 808, 179
Foreman-Mackey, D. 2016, JOSS, 1, 24
Foreman-Mackey, D., Hogg, D. W., Lang, D., & Goodman, J. 2013, PASP, 125, 306
Gaia Collaboration, Brown, A. G. A., Vallenari, A., et al. 2018, A&A, 616, A1
Geier, S., Raddi, R., Gentile Fusillo, N. P., & Marsh, T. R. 2019, A&A, 621, A38
Giddings, J. R. 1981, PhD thesis, Univ. London
Guidry, J. A., Vanderbosch, Z. P., Hermes, J. J., et al. 2021, ApJ, 912, 125
Han, Z., Podsiadlowski, P., Maxted, P. F. L., & Marsh, T. R. 2003, MNRAS, 341, 669
Han, Z., Podsiadlowski, P., Maxted, P. F. L., Marsh, T. R., & Ivanova, N. 2002, MNRAS, 336, 449
Heber, U. 2016, PASP, 128, 082001
Hubeny, I., Hummer, D. G., & Lanz, T. 1994, A&A, 282, 151
Irrgang, A., Kreuzer, S., Heber, U., & Brown, W. 2018, A&A, 615, L5
Ivanova, N., Justham, S., Chen, X., et al. 2013, A&ARv, 21, 59
Kilkenny, D. 2014, MNRAS, 445, 4247
Kilkenny, D., Hilditch, R. W., & Penfold, J. E. 1978, MNRAS, 183, 523
Kurucz, R. L. 1996, in Model Atmospheres and Spectrum Synthesis, ed. S. J. Adelman, F. Kupka, & W. W. Weiss (San Francisco: ASP), 160
Lightkurve Collaboration, Cardoso, J. V. d. M., Hedges, C., et al. 2018, Lightkurve: Kepler and TESS time series analysis in Python, Astrophysics Source Code Library, ascl:1812.013
Lucy, L. B. 1967, ZAp, 65, 89
Maxted, P. F. L., Heber, U., Marsh, T. R., & North, R. C. 2001, MNRAS, 326, 1391
Napiwotzki, R., Green, P. J., & Saffer, R. A. 1999, ApJ, 517, 399
Naslim, N., Jeffery, C. S., Hibbert, A., & Behara, N. T. 2013, MNRAS, 434, 1920
Nieva, M. F., & Przybilla, N. 2008, A&A, 481, 199
Parsons, S. G., Gänsicke, B. T., Marsh, T. R., et al. 2018, MNRAS, 481, 1083
Parsons, S. G., Marsh, T. R., Copperwheat, C. M., et al. 2010, MNRAS, 402, 2591
Pietrukowicz, P., Mróz, P., Soszyński, I., et al. 2013, AcA, 63, 115
Press, W. H., Teukolsky, S. A., Vetterling, W. T., & Flannery, B. P. 1992, Numerical recipes in FORTRAN. The art of scientific computing (2nd edn.; Cambridge: Cambridge Univ. Press)
Przybilla, N., Butler, K., Becker, S. R., & Kudritzki, R. P. 2006a, A&A, 445, 1099
Przybilla, N., Nieva, M. F., & Edelmann, H. 2006b, BaltA, 15, 107
Saffer, R. A., Bergeron, P., Koester, D., & Liebert, J. 1994, ApJ, 432, 351
Sahoo, S. K., Baran, A. S., Sanjayan, S., & Ostrowski, J. 2020, MNRAS, 499, 5508
Scargle, J. D. 1982, ApJ, 263, 835
Schaffenroth, V., Barlow, B. N., Drechsel, H., & Dunlap, B. H. 2015, A&A, 576, A123
Schaffenroth, V., Barlow, B. N., Geier, S., et al. 2019, A&A, 630, A80
Schaffenroth, V., Casewell, S. L., Schneider, D., et al. 2021, MNRAS, 501, 3847
Schaffenroth, V., Classen, L., Nagel, K., et al. 2014a, A&A, 570, A70
Schaffenroth, V., Geier, S., Drechsel, H., et al. 2013, A&A, 553, A18
Schaffenroth, V., Geier, S., Heber, U., et al. 2014b, A&A, 564, A98
Soker, N. 1998, AJ, 116, 1308
Soszyński, I., Stępień, K., Pilecki, B., et al. 2015, AcA, 65, 39
Tody, D. 1986, Proc. SPIE, 627, 733
Tody, D. 1993, in ASP Conf. Ser. 52, Astronomical Data Analysis Software and Systems II, ed. R. J. Hanisch, R. J. V. Brissenden, & J. Barnes (San Francisco, CA: ASP), 173
Tonry, J. L., Denneau, L., Heinze, A. N., et al. 2018, PASP, 130, 064505
Tremblay, P. E., & Bergeron, P. 2009, ApJ, 696, 1755
Virtanen, P., Gommers, R., Oliphant, T. E., et al. 2020, NatMe, 17, 261
von Zeipel, H. 1924, MNRAS, 84, 665
Vos, J., Vučković, M., Chen, X., et al. 2019, MNRAS, 482, 4592